Available online at www.sciencedirect.com
ScienceDirect
Comput. Methods Appl. Mech. Engrg. 197 (2008) 1699–1714
Computer methods in applied mechanics and engineering
www.elsevier.com/locate/cma

An eXtended Finite Element Method/Lagrange multiplier based approach for fluid–structure interaction

Axel Gerstenberger, Wolfgang A. Wall *

Chair for Computational Mechanics, Technische Universität München, Boltzmannstr. 15, 85747 Garching, Germany

Received 19 February 2007; received in revised form 30 June 2007; accepted 5 July 2007
Available online 25 July 2007

Abstract

This paper presents a new fixed grid fluid–structure interaction scheme that can be applied to the interaction of most general structures with incompressible flow. It is based on an eXtended Finite Element Method (XFEM) based strategy. The extended Eulerian fluid field and the Lagrangian structural field are partitioned and iteratively coupled using Lagrange multiplier techniques for non-matching grids. The approach allows the simulation of the interaction of thin and bulky structures exhibiting large deformations. Finally, qualitative examples and a benchmark computation demonstrate key features and accuracy of the method.

Keywords: Fluid–structure interaction; eXtended Finite Element Method; Fixed grid; Domain decomposition; Mortar method; Lagrange multiplier

1. Introduction

Fluid–structure interaction is of great relevance in many fields of engineering as well is in the applied sciences. Hence the development and application of respective simulation approaches has gained great attention over the past decades. Some current endeavors in this field are: the advancement from special purpose or special problem to quite general approaches; the desire to even capture very general and complex systems; and the exigent need of robust high quality approaches even for such complex cases, *i.e.* approaches that have the potential to turn over from being a challenging and fascinating research topic to a development tool with real predictive capabilities [43]. Often, when interaction effects are essential this comes along with large structural deformations. However, many available approaches (both in research as well as in commercial codes) lack robustness especially in this situation.

A sketch of the general problem of the interaction of a flow field and a flexible structure is shown in Fig. 1. The interface Γ^{i} separates the structural domain Ω^{s} from the fluid domain Ω^{f}. Most research and commercial codes that are available for simulations of the interaction of flows and flexible, often thin-walled, structures are based on the Arbitrary Lagrangian Eulerian (ALE) method. These approaches go back to early works like [3,4,12,20,22,33]. The essential feature of ALE based methods is that the fluid field is formulated and solved on a deforming grid. This grid deforms with the structure at the interface and then the grid deformation is extended into the fluid field.

But even the most advanced and best cultured ALE based scheme once comes to its limits where only re-meshing helps. At the latest in such situations, one might be tempted to turn over to approaches that work with a fixed grid. Here, the interface is described either explicitly, using some kind of Lagrangian interface markers or a Lagrangian structural discretization, or implicitly, using *e.g.* level-set functions on a fixed fluid grid. Changing properties and discontinuities in the fluid solution have to be taken care of with modifications on the fluid equations and/or fluid discretization.

* Corresponding author. Tel.: +49 89 289 15300; fax: +49 89 289 15301.
E-mail address: wall@lnm.mw.tum.de (W.A. Wall).
URLs: http://www.lnm.mw.tum.de/ (A. Gerstenberger), http://www.lnm.mw.tum.de/ (W.A. Wall).

0045-7825/$ - see front matter © 2007 Elsevier B.V. All rights reserved.
doi:10.1016/j.cma.2007.07.002

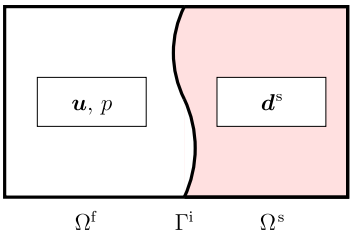

Fig. 1. Problem setup: fluid field Ω^f, structural field Ω^s and the conjoined interface Γ^i.

Prominent fixed grid methods for incompressible flow include the Immersed Boundary (IB) method [35,36] and its many derivations [24,26,28]. It is capable to simulate thin and deformable boundaries and fully fledged, deformable 3d structures submersed in incompressible flow [45,48]. An approach with many similarities to the IB method is the so called Distributed Lagrange Multiplier/Fictitious Domain (DLM/FD) method [17,18]. Originally, the approach was developed for rigid particles with translational and rotational degrees of freedom. The DLM/FD methods have since been extended to simulate thin, deformable structural surfaces [1,11,40] as well as to flexible and fully fledged structures [47]. Both methods have in common a Lagrangian mesh for the structure moving on top of the fluid mesh and forcing the fluid material inside the structure to deform as the structure. Other fixed grid or Cartesian grid methods are, among others, Fedkiw et al. [13], Cirak and Radovitzky [9] and Löhner et al. [27].

One very attractive feature of ALE methods is that fluid and structure domain can be discretized each on its own such that one only has to deal with the coupling of fitting or non-fitting surface meshes. However, when treating a structure on a fixed-fluid grid, the fluid–structure interface essentially divides the fluid domain in a physical flow field and a fictitious field that may be discretized and solved, but has no physical meaning to the FSI problem.

The problem with most fixed grid methods is that there is no way to decouple physical and fictitious domain properly with respect to the kinematic and stress fields and switch of the fictitious flow field calculation to reduce unnecessary computations. In most DLM/FD and IB approaches to date, if used with volume occupying structures, the coupling takes place between the fictitious flow field and the structure domain, not the surface. Since the structure movement is tied to the fictitious flow, it is forced to deform in an incompressible way and artificial viscosity modifies the real physics of the structural domain. Of course the error made by such coupling might not be prohibitive high in specific situations, however, it still poses additional sources of errors for an already complex physical problem.

In summary we propose a number of requirements that future fixed grid methods have to fulfill to be applicable to general structures interacting with incompressible flow: the physical and fictitious flow region are physically decoupled such that no energy transfer occurs across the interface, the coupling takes place only along the interface, there is no mesh size dependency between fluid and structure mesh and it should be possible to turn off most parts of the fictitious domain in order to reduce memory and performance consumption. Despite of the fluid mesh deformation problem, ALE methods, when properly implemented, could be seen as a reference in terms of applicability, accuracy and numerical stability as well as generality with respect to structural material models.

In an attempt to meet all of these requirements, we propose a partitioned iterative coupling scheme between a standard Lagrangian structural description and an Eulerian formulation for the fluid that uses features of the eXtended Finite Element Method (XFEM) and DLM/FD methods mentioned above. A related monolithic implementation of another XFEM based approach for compressible flows was published in Legay et al. [25]. The XFEM was originally introduced for the simulation of cracks and other discontinuities in structures [2,32] and has been, close to the topic at hand, extended to problems of two-phase flow [8] and Stokes flow/rigid particle interaction [41]. In this paper, we derive a 3-field FSI approach with an intermediate reference field. The 3-field approach greatly increases the flexibility with respect to discretization techniques and code modularity.

With this XFEM based approach for the fluid, in principal all of the mentioned shortcoming can be addressed, most prominently, there is no influence of the fictitious fluid domain anymore and, for a sufficient large fictitious fluid domain, a significant number of unnecessary fluid unknowns can be removed. The interface can properly represent the discontinuities. The issue of mesh size dependency between fluid and solid mesh can be shifted to an issue of choosing the right lagrange multiplier method [6,7], which itself is a vivid research topic in the domain decomposition community.

The paper is structured as follows: The general FSI problem is stated in Section 2, where we also propose our 3-field approach. The introduction of the intermediate interface field as an external reference allows us to derive the XFEM fluid problem and its coupling to the interface in Section 3 separately from the coupling between structure and interface, which is subsequently described in Section 4. The coupling and the overall solution approach is then derived in Section 5. Finally, we provide example computations to illustrate important aspects and features of the proposed algorithm and a first 'benchmark' computation to verify the correct transfer of physical quantities across the fluid–structure interface in Section 6.

2. Statement of coupled fluid–structure problem

A general fluid–structure interaction problem statement consists of the description of fluid and solid fields, appropriate fluid–structure interface conditions at the common interface and conditions for the remaining boundaries, respectively.

2.1. Fluid

For the fluid domain Ω^{f} with the position vector $\boldsymbol{x}$, the conservation of momentum is stated as

$$\rho^{\mathrm{f}} \frac{\mathrm{D}\boldsymbol{u}}{\mathrm{D}t} = \nabla \cdot \boldsymbol{\sigma}^{\mathrm{f}} + \rho^{\mathrm{f}} \boldsymbol{b}^{\mathrm{f}} \quad \forall \boldsymbol{x} \in \Omega^{\mathrm{f}}. \tag{1}$$

Here, the material time derivative of the fluid velocity $\boldsymbol{u}$ times the fluid density ρ^{f} is balanced by the divergence of the Cauchy stress tensor $\boldsymbol{\sigma}^{\mathrm{f}}$ and external, velocity independent volumetric forces $\boldsymbol{b}^{\mathrm{f}}$. For brevity, the volumetric forces are omitted in the subsequent derivation, however they are included in the actual implementation and their derivation requires no additional difficulties. Mass conservation for an incompressible fluid is stated as

$$\nabla \cdot \boldsymbol{u} = 0. \tag{2}$$

We use the Newtonian material law, which defines the internal stress tensor $\boldsymbol{\sigma}^{\mathrm{f}}$ as

$$\boldsymbol{\sigma}^{\mathrm{f}} = -p\boldsymbol{I} + 2\mu\boldsymbol{\varepsilon}(\boldsymbol{u}). \tag{3}$$

It is composed from the pressure p and a product of the dynamic viscosity denoted as μ and the strain rate tensor $\boldsymbol{\varepsilon}$ given by

$$\boldsymbol{\varepsilon}(\boldsymbol{u}) = \frac{1}{2}(\nabla \boldsymbol{u} + (\nabla \boldsymbol{u})^{\mathrm{T}}). \tag{4}$$

The specific form of the material time derivative depends on the choice of the reference system that is employed to formulate the problem. The choice of a specific reference system is inspired by the way the moving interface is treated. There are basically three alternative reference systems: the Eulerian, the Lagrangian and the Arbitrary Lagrangian Eulerian (ALE) formulation. For fixed grid methods as used in this work, an Eulerian formulation is used. In this case the material time derivative is given as the sum of a local time derivative plus a convective term. Hence, the momentum equation reads as

$$\rho^{\mathrm{f}} \dot{\boldsymbol{u}} = -\rho^{\mathrm{f}} \boldsymbol{u} \cdot \nabla \boldsymbol{u} - \nabla p + 2\mu \nabla \cdot \boldsymbol{\varepsilon}(\boldsymbol{u}), \tag{5}$$

$$\nabla \cdot \boldsymbol{u} = 0, \tag{6}$$

where the dot over the velocity indicates a partial derivative with respect to time.

Furthermore, the Dirichlet and Neumann fluid boundary conditions at $\Gamma^{\mathrm{f,Neu}}$ and $\Gamma^{\mathrm{f,Dir}}$ are given as

$$\boldsymbol{u} = \bar{\boldsymbol{u}} \quad \forall \boldsymbol{x} \in \Gamma^{\mathrm{f,Dir}}, \tag{7}$$

$$\boldsymbol{\sigma}^{\mathrm{f}} \cdot \boldsymbol{n}^{\mathrm{f}} = \bar{\boldsymbol{h}}^{\mathrm{f}} \quad \forall \boldsymbol{x} \in \Gamma^{\mathrm{f,Neu}}. \tag{8}$$

The bar above a variable indicates that this field is a known or prescribed boundary condition for the fluid computation.

Without consideration of a moving interface, the weak form of the Navier–Stokes equation in Eulerian form, after integration by parts, becomes

$$(\boldsymbol{v}, \rho^{\mathrm{f}} \dot{\boldsymbol{u}})_{\Omega^{\mathrm{f}}} + (\boldsymbol{v}, \rho^{\mathrm{f}} \boldsymbol{u} \cdot \nabla \boldsymbol{u})_{\Omega^{\mathrm{f}}} + \left(\nabla \cdot \boldsymbol{v}, \boldsymbol{\sigma}^{\mathrm{f}}\right)_{\Omega^{\mathrm{f}}} + (q, \nabla \cdot \boldsymbol{u})_{\Omega^{\mathrm{f}}} - (\boldsymbol{v}, \bar{\boldsymbol{h}}^{\mathrm{f}})_{\Gamma^{\mathrm{f,Neu}}} = 0. \tag{9}$$

Such a formulation is known to show instabilities for two reasons – dominating convection and (inf–sup) unstable pairs of velocity and pressure shape functions. In this work we mainly use quadratic order shape functions for velocity and pressure space discretization. The employed GLS-stabilization is characterized by a modification of the discrete test functions $\boldsymbol{v}^{\mathrm{h}}$ and p^{h} given as

$$\boldsymbol{v}^{\mathrm{mod,h}} = \boldsymbol{v}^{\mathrm{h}} + \tau^{\mathrm{M}}[\rho^{\mathrm{f}} \boldsymbol{u}^{\mathrm{h}} \cdot \nabla \boldsymbol{v}^{\mathrm{h}} + \nabla q - 2\mu \nabla \cdot \boldsymbol{\varepsilon}(\boldsymbol{v}^{\mathrm{h}})], \tag{10}$$

$$q^{\mathrm{mod,h}} = q^{\mathrm{h}} + \tau^{\mathrm{C}}[\nabla \cdot \boldsymbol{v}^{\mathrm{h}}]. \tag{11}$$

Following Wall [42], the stabilization parameters τ^{M} and τ^{C} for each element K are given as

$$\tau^{\mathrm{M}} = \min\left[\Delta t, \frac{h_K}{2|\boldsymbol{u}^{\mathrm{h}}|_{p=2}}, \frac{m_K h_K^2 \rho^f}{4\mu}\right], \tag{12}$$

$$\tau^{\mathrm{C}} = \frac{|\boldsymbol{u}^{\mathrm{h}}|_{p=2} h_K}{2} \xi(Re), \tag{13}$$

with

$$\xi(Re) = \begin{cases} Re_K, & 0 \leqslant Re < 1, \\ 1, & Re_K \geqslant 1. \end{cases} \tag{14}$$

The element Reynolds number Re_K is defined as

$$Re_K = \frac{m_K |\boldsymbol{u}^{\mathrm{h}}|_{p=2} h_K \rho^{\mathrm{f}}}{2\mu}. \tag{15}$$

For quadratic order shape functions we use $m_K = 1/12$. The necessary element size h_K is evaluated at each integration point using the approximate streamlength approach.

2.2. Structure

In most applications, the structure is described using a Lagrangian description, where the material derivative becomes a simple partial derivative with respect to time, such that

$$\rho^{\mathrm{s}} \frac{\partial^2 \boldsymbol{d}^{\mathrm{s}}}{\partial t^2} = \nabla \cdot \boldsymbol{\sigma}^{\mathrm{s}} + \rho^{\mathrm{s}} \boldsymbol{b}^{\mathrm{s}}, \tag{16}$$

with the displacement $\boldsymbol{d}^{\mathrm{s}}$ defined as the difference between the current position $\boldsymbol{x}$ and the initial position $\boldsymbol{x}_0$ and $\boldsymbol{b}^{\mathrm{s}}$ being an external acceleration field acting on the structural domain. The structural velocity $\boldsymbol{u}^{\mathrm{s}}$ and acceleration $\boldsymbol{a}^{\mathrm{s}}$ are defined as

$$\boldsymbol{a}^{\mathrm{s}} = \frac{\partial \boldsymbol{u}^{\mathrm{s}}}{\partial t} = \frac{\partial^2 \boldsymbol{d}^{\mathrm{s}}}{\partial t^2} \quad \text{or} \quad \boldsymbol{a}^{\mathrm{s}} = \dot{\boldsymbol{u}}^{\mathrm{s}} = \ddot{\boldsymbol{d}}^{\mathrm{s}}. \tag{17}$$

In the large deformation case it is common to describe the constitutive equation using a stress–strain relation based on the Green–Lagrange strain tensor $\boldsymbol{E}$ and the 2. Piola–Kirchhoff stress tensor $\boldsymbol{S}(\boldsymbol{E})$ as a function of $\boldsymbol{E}$. The 2. Piola–Kirchhoff stress can be obtained from the Cauchy stress $\boldsymbol{\sigma}$ as

$$\boldsymbol{S} = J\boldsymbol{F}^{-1}\cdot\boldsymbol{\sigma}\cdot\boldsymbol{F}^{-\mathrm{T}} \tag{18}$$

and the Green–Lagrange strain tensor $\boldsymbol{E}$ as

$$\boldsymbol{E} = \frac{1}{2}(\boldsymbol{F}^{\mathrm{T}}\cdot\boldsymbol{F} - \boldsymbol{I}). \tag{19}$$

J denotes the determinant of the deformation gradient tensor $\boldsymbol{F}$, which itself is defined as

$$\boldsymbol{F} = \frac{\partial \boldsymbol{x}}{\partial \boldsymbol{x}_0}. \tag{20}$$

The equation of motion with respect to the reference configuration then reads

$$\rho_0^{\mathrm{s}}\ddot{\boldsymbol{d}}^{\mathrm{s}} = \nabla\cdot(\boldsymbol{S}^{\mathrm{s}}\cdot\boldsymbol{F}^{\mathrm{T}}) + \rho_0^{\mathrm{s}}\boldsymbol{b}^{\mathrm{s}}, \tag{21}$$

where ρ_0^{s} is the density of the reference domain. For the numerical results presented in this article we use the St.-Venant–Kirchhoff material law, *i.e.* a linear relation between $\boldsymbol{S}$ and $\boldsymbol{E}$, for simplicity.

The complete strong form, where we omit the body forces for brevity, can be given by

$$\rho^{\mathrm{s}}\ddot{\boldsymbol{d}}^{\mathrm{s}} = \nabla\cdot\boldsymbol{\sigma}^{\mathrm{s}} \quad \forall \boldsymbol{x}\in\Omega^{\mathrm{s}}, \tag{22}$$

$$\boldsymbol{\sigma}^{\mathrm{f}}\cdot\boldsymbol{n}^{\mathrm{f}} = \bar{\boldsymbol{h}}^{\mathrm{s}} \quad \forall \boldsymbol{x}\in\Gamma^{\mathrm{s,Neu}}, \tag{23}$$

$$\boldsymbol{d}^{\mathrm{s}} = \bar{\boldsymbol{d}}^{\mathrm{s}} \quad \forall \boldsymbol{x}\in\Gamma^{\mathrm{s,Dir}} \tag{24}$$

plus initial conditions for the structural displacements

$$\boldsymbol{d}^{\mathrm{s}}(\boldsymbol{x}, t=0) = \boldsymbol{d}_0^{\mathrm{s}}. \tag{25}$$

The weak from after integration by parts without consideration of the coupling is

$$(\delta\boldsymbol{d}^{\mathrm{s}}, \rho^{\mathrm{s}}\ddot{\boldsymbol{d}}^{\mathrm{s}})_{\Omega^{\mathrm{s}}} + (\nabla\delta\boldsymbol{d}^{\mathrm{s}}, \boldsymbol{\sigma}^{\mathrm{s}})_{\Omega^{\mathrm{s}}} - (\delta\boldsymbol{d}^{\mathrm{s}}, \bar{\boldsymbol{h}}^{\mathrm{s}})_{\Gamma^{\mathrm{s,Neu}}} = 0. \tag{26}$$

The equation is discretized using different (hybrid–mixed) element techniques in space and direct time integration schemes. Nonlinearities are handled via a Newton–Raphson scheme. Some further remarks on spatial and time discretization aspects are given Section 4.

2.3. Fluid–structure interface conditions

The main conditions at the interface are the dynamic and kinematic coupling conditions. We assume no mass flow across the interface. Consequently, the normal velocities at the interface have to match as

$$\boldsymbol{u}\cdot\boldsymbol{n}^{\mathrm{f}} = -\dot{\boldsymbol{d}}^{\mathrm{s}}\cdot\boldsymbol{n}^{\mathrm{s}} \quad \forall \boldsymbol{x}\in\Gamma^{\mathrm{i}}. \tag{27}$$

Note the opposite sign due to the different normal vector $\boldsymbol{n}^{\mathrm{f}}$ and $\boldsymbol{n}^{\mathrm{s}}$ for fluid and structural domain, respectively (Fig. 2). If viscous fluids are considered, there is usually also a matching condition for the tangential velocities, which can be combined with the equation above to obtain the 'no slip' boundary conditions as

$$\boldsymbol{u} = \dot{\boldsymbol{d}}^{\mathrm{s}} \quad \forall \boldsymbol{x}\in\Gamma^{\mathrm{i}}. \tag{28}$$

The force equilibrium requires the surface traction to be equal as

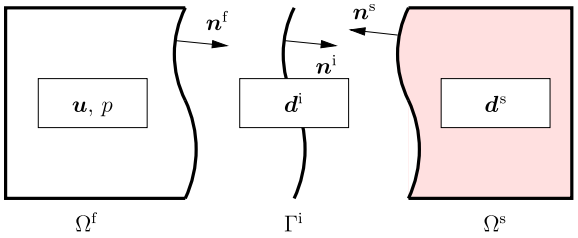

Fig. 2. 3-field setup: fluid field Ω^{f}, interface Γ^{i} and structural field Ω^{s} along with respective domain normals and variables.

$$\boldsymbol{\sigma}^{\mathrm{f}}\cdot\boldsymbol{n}^{\mathrm{f}} = -\boldsymbol{\sigma}^{\mathrm{s}}\cdot\boldsymbol{n}^{\mathrm{s}} \quad \forall \boldsymbol{x}\in\Gamma^{\mathrm{i}}. \tag{29}$$

It is important to note the position of Γ^{i} is obviously varying with time and is only defined through the interaction of both fields.

2.4. Introduction of the 3-field problem

The interface conditions have to be applied along a moving surface, which is no problem when Lagrangian formulations are used as for the structure. For the fluid field, ALE methods were invented that allow the fluid mesh to move independently from the flow field. This allows the fluid surface to follow the interface. In a pure Eulerian description, there is no moving boundary one could couple the moving interface with. One has to introduce a separate interface description. Such an interface can separate two areas of the flow field: one that correspond to the physical flow field and one that is completely fictitious.

For maximum flexibility with respect to choice of approximation functions, mesh size and solution techniques, we propose a 3-field setup, where fluid and structural fields and an independent interface field are treated separately. This setup – along with the respective variables living on these fields or interfaces – is shown in Fig. 2. Similar ideas for coupling 2 fields using an intermediate reference surface ('frame') can be found *e.g.* in Park et al. [34] and references therein.

For the 3-field problem, the interface condition Eq. (28) is modified as

$$\boldsymbol{u} = \dot{\boldsymbol{d}}^{\mathrm{i}}, \tag{30}$$

$$\boldsymbol{d}^{\mathrm{i}} = \boldsymbol{d}^{\mathrm{s}}. \tag{31}$$

In other words, if we constrain the velocity of both fields independently to be the same as the interface velocity, then the original matching condition (28) is fulfilled. Let $\boldsymbol{\lambda}$ and $\boldsymbol{\mu}$ be two traction fields on the interface Γ^{i} such that

$$\boldsymbol{\sigma}^{\mathrm{f}}\cdot\boldsymbol{n}^{\mathrm{f}} = \boldsymbol{\lambda}, \tag{32}$$

$$\boldsymbol{\sigma}^{\mathrm{s}}\cdot\boldsymbol{n}^{\mathrm{s}} = \boldsymbol{\mu}. \tag{33}$$

Then the interface traction balance (29) can be stated as

$$\boldsymbol{\lambda} = -\boldsymbol{\mu}. \tag{34}$$

Since we generally assume that neither fluid nor structural discretization match the interface mesh, we need to couple three non-fitting meshes. The single fields can now be described separately using the coupling of each field to the interface. During this derivation, the interface serves as a reference field with given position and velocity in time. The complete system will be treated in Section 5.

3. Moving fluid boundaries and interfaces on fixed Eulerian grids

3.1. Definition of the fluid problem

The key element of the proposed FSI approach is to properly define moving interfaces on a fixed Eulerian fluid grid. For that purpose, we define a domain Ω that contains the fluid domain Ω^{f} completely and extends into the structural domain Ω^{s}. The interface between fluid and structure becomes now an internal interface that separates Ω into two subdomains Ω^{+} and Ω^{-}, where Ω^{+} corresponds to the *physical* fluid domain Ω^{f} and Ω^{-} is the remaining domain filling Ω. Hence, the flow field in Ω^{-} is entirely *fictitious* with no physical meaning to the FSI problem.

The main tasks are to decouple the physical flow in Ω^{+} and the fictitious flow in Ω^{-} and, using the new 3-field setup, to employ the interface conditions between the interface and the physical flow in Ω^{+}. Only then the physical behavior is correctly covered. For easier reference, we define two additional names for the boundary Γ^{i}, namely Γ^{+} and Γ^{-}, depending on whether functions are evaluated approaching Γ^{i} from Ω^{+} or Ω^{-}, respectively. The principle setup of the proposed approach is depicted in Fig. 3.

The kinematic conditions along the interface are now valid boundary conditions only for Ω^{+} such that

$$\boldsymbol{u} = \bar{\boldsymbol{u}}^{\mathrm{i}} \quad \forall \boldsymbol{x} \in \Gamma^{+}. \tag{35}$$

For Ω^{-}, the entire boundary shall be a Neumann boundary with zero traction applied as

$$\boldsymbol{\sigma}^{\mathrm{f}} \cdot \boldsymbol{n} = \boldsymbol{0} \quad \forall \boldsymbol{x} \in \Gamma^{-}. \tag{36}$$

Fulfilling both conditions along Γ^{i} requires us to introduce a discontinuous velocity and stress field, which will be done during the discretization process.

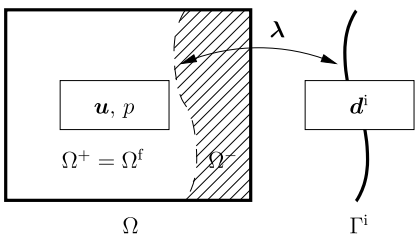

Fig. 3. Fluid part of the FSI problem: Γ^{i} separates the computational fluid domain Ω in a physical fluid domain Ω^{+} corresponding to Ω^{f} and the 'fictitious' fluid domain Ω^{-}. Interface velocity and position are constrained using a Lagrange multiplier field $\boldsymbol{\lambda}$.

The initial conditions are given as

$$\boldsymbol{u}(\boldsymbol{x}, t=0) = \boldsymbol{u}^{0} \quad \forall \boldsymbol{x} \in \Omega^{+}, \tag{37}$$

$$p(\boldsymbol{x}, t=0) = p^{0} \quad \forall \boldsymbol{x} \in \Omega^{+}, \tag{38}$$

$$\boldsymbol{u}(\boldsymbol{x}, t=0) = \boldsymbol{0} \quad \forall \boldsymbol{x} \in \Omega^{-}, \tag{39}$$

$$p(\boldsymbol{x}, t=0) = 0 \quad \forall \boldsymbol{x} \in \Omega^{-}. \tag{40}$$

Body forces, if present, are only applied to Ω^{+}.

With this set of boundary and initial conditions and a properly decoupled flow field between Ω^{+} and Ω^{-}, there will be zero velocity and pressure in Ω^{-} at all times.

3.2. Discretization in time

For simplicity of presentation, the one-step-θ time discretization is employed in the following. In the one-step-θ method, the acceleration $\dot{\boldsymbol{u}}$ is defined as a combination of the acceleration at the new and the old time step

$$\frac{\boldsymbol{u}^{n+1} - \boldsymbol{u}^{n}}{\Delta t} = \theta \dot{\boldsymbol{u}}^{n+1} + (1-\theta)\dot{\boldsymbol{u}}^{n}. \tag{41}$$

Likewise, the pressure is discretized in time as

$$p^{n+\theta} = \theta p^{n+1} + (1-\theta) p^{n}. \tag{42}$$

Sorting Eq. (41) for expressions at the new time step $n+1$ and the old time step n gives

$$\boldsymbol{u}^{n+1} - \Delta t \theta \dot{\boldsymbol{u}}^{n+1} = \boldsymbol{u}^{n} + \Delta t (1-\theta)\dot{\boldsymbol{u}}^{n}. \tag{43}$$

Now $\dot{\boldsymbol{u}}^{n+1}$ can be replaced by the right hand side of Eq. (5) evaluated at the new time step $n+1$

$$\boldsymbol{u}^{n+1} + \Delta t \theta \left[\boldsymbol{u} \cdot \nabla \boldsymbol{u} - \frac{1}{\rho^{\mathrm{f}}} \nabla \cdot \boldsymbol{\sigma}^{\mathrm{f}} \right]^{n+1} = \boldsymbol{u}^{n} + \Delta t (1-\theta)\dot{\boldsymbol{u}}^{n} \tag{44}$$

in Ω. For the complete time-discrete strong form for the fluid flow in Ω^{+} and Ω^{-} we also require

$$\nabla \cdot \boldsymbol{u}^{n+1} = 0. \tag{45}$$

The semi-discrete equation combined with the already defined boundary and initial conditions form the basis for the subsequent spatial discretization.

3.3. Weak form of the time-discrete flow equation system

The weak form is developed by multiplying Eq. (44) and Eq. (45) with the velocity and pressure test functions $\boldsymbol{v}$ and q, respectively

$$\begin{aligned} &\left[(\boldsymbol{v}, \rho^{\mathrm{f}} \boldsymbol{u})_{\Omega} + \Delta t \theta \left\{ (\boldsymbol{v}, \rho^{\mathrm{f}} \boldsymbol{u} \cdot \nabla \boldsymbol{u} - \nabla \cdot \boldsymbol{\sigma}^{\mathrm{f}})_{\Omega} + (q, \nabla \cdot \boldsymbol{u})_{\Omega} \right\} \right]^{n+1} \\ &\quad = (\boldsymbol{v}, \rho^{\mathrm{f}} \boldsymbol{u}^{n})_{\Omega} + \Delta t (1-\theta)(\boldsymbol{v}, \rho^{\mathrm{f}} \dot{\boldsymbol{u}}^{n})_{\Omega}. \end{aligned} \tag{46}$$

The fluid–structure interface condition (35) is enforced weakly by testing the condition with a test function $\delta\boldsymbol{\lambda}(\boldsymbol{x})$ along the interface as

$$\begin{aligned} &[(\boldsymbol{v}, \rho^{\mathrm{f}} \boldsymbol{u})_{\Omega} + \Delta t \theta \{ (\boldsymbol{v}, \rho^{\mathrm{f}} \boldsymbol{u} \cdot \nabla \boldsymbol{u} - \nabla \cdot \boldsymbol{\sigma}^{\mathrm{f}})_{\Omega} + (q, \nabla \cdot \boldsymbol{u})_{\Omega} \\ &\quad - (\delta\boldsymbol{\lambda}, \boldsymbol{u} - \bar{\boldsymbol{u}}^{\mathrm{i}})_{\Gamma^{+}} \}]^{n+1} \\ &\quad = (\boldsymbol{v}, \rho^{\mathrm{f}} \boldsymbol{u}^{n})_{\Omega} + \Delta t (1-\theta)(\boldsymbol{v}, \rho^{\mathrm{f}} \dot{\boldsymbol{u}}^{n})_{\Omega}. \end{aligned} \tag{47}$$

This is necessary, since we cannot apply Eq. (35) directly as Dirichlet conditions due to the non-fitting fluid and interface meshes. It should be clear from Eq. (47) that the coupling condition is weakly enforced at t^{n+1} at the t^{n+1} location of the interface Γ^{i}. Integration by parts of the stress term yields

$$-(\boldsymbol{v}, \nabla \cdot \boldsymbol{\sigma}^{\mathrm{f}})_{\Omega} = -(\boldsymbol{v}, \boldsymbol{\sigma}^{\mathrm{f}} \cdot \boldsymbol{n}^{\mathrm{f}})_{\Gamma} + (\nabla \cdot \boldsymbol{v}, \boldsymbol{\sigma}^{\mathrm{f}})_{\Omega}. \tag{48}$$

For Dirichlet boundary conditions, the surface integral vanishes due to the vanishing test function. Neumann conditions are applied by letting $\boldsymbol{\sigma}^{\mathrm{f}} \cdot \boldsymbol{n}^{\mathrm{f}} = \bar{\boldsymbol{h}}^{\mathrm{f}}$.

Already from a dimensional analysis we see that $\delta\boldsymbol{\lambda}$ has to be a kind of traction vector. In our particular setup, where velocities and pressure jump from zero in Ω^- to their physical values in Ω^+, the traction corresponds to real reaction, as if an ordinary domain boundary would be at this place. Therefore, on Γ^+, $\boldsymbol{\sigma}^{\mathrm{f}} \cdot \boldsymbol{n}^{\mathrm{f}}$ can be defined as the Lagrange multiplier field $\boldsymbol{\lambda}$ such that

$$-(\boldsymbol{v}, \nabla \cdot \boldsymbol{\sigma}^{\mathrm{f}})_{\Omega} = -(\boldsymbol{v}, \bar{\boldsymbol{h}}^{\mathrm{f}})_{\Gamma^{\mathrm{f,Neu}}} - (\boldsymbol{v}, \boldsymbol{\lambda})_{\Gamma^+} + (\nabla \cdot \boldsymbol{v}, \boldsymbol{\sigma}^{\mathrm{f}})_{\Omega}. \tag{49}$$

The velocity matching condition $(\delta\boldsymbol{\lambda}, \boldsymbol{u} - \bar{\boldsymbol{u}}^{\mathrm{i}})_{\Gamma^+}$ in Eq. (47) was multiplied by $\Delta t\theta$, which is possible since $\delta\boldsymbol{\lambda}(\boldsymbol{x})$ is an arbitrary test function. This factor allows us to identify $\delta\boldsymbol{\lambda}(\boldsymbol{x})$ as the test function for the Lagrange multiplier (or traction) field $\boldsymbol{\lambda}(\boldsymbol{x})$ with consistent physical units and results in symmetric stiffness submatrices for the Lagrange multiplier formulation.

The Dirichlet and Neumann conditions away from the interface are employed as usual, therefore, we will not include the Neumann boundary term in the following derivation for the sake of clarity.

Inserting Eq. (49) and reordering Eq. (47) for unknown and known expressions, the final weak form is

$$\begin{aligned}
&[(\boldsymbol{v}, \rho^{\mathrm{f}}\boldsymbol{u})_{\Omega} + \Delta t\theta\{(\boldsymbol{v}, \rho^{\mathrm{f}}\boldsymbol{u} \cdot \nabla\boldsymbol{u})_{\Omega} + (\nabla \cdot \boldsymbol{v}, \boldsymbol{\sigma}^{\mathrm{f}})_{\Omega} + (q, \nabla \cdot \boldsymbol{u})_{\Omega} \\
&\quad - (\boldsymbol{v}, \boldsymbol{\lambda})_{\Gamma^+} - (\delta\boldsymbol{\lambda}, \boldsymbol{u})_{\Gamma^+}\}]^{n+1} \\
&\quad = (\boldsymbol{v}, \rho^{\mathrm{f}}\boldsymbol{u}^n)_{\Omega} + \Delta t(1-\theta)(\boldsymbol{v}, \rho^{\mathrm{f}}\dot{\boldsymbol{u}}^n)_{\Omega} - \Delta t\theta(\delta\boldsymbol{\lambda}, \bar{\boldsymbol{u}}^{\mathrm{i},n+1})_{\Gamma^+}.
\end{aligned} \tag{50}$$

It is important to stress the fact that the velocity matching condition along Γ^+ is only enforced for the velocity field in Ω^+. For the velocity field in Ω^-, the interface represents a Neumann condition. Hence, the movement of the interface does not affect the flow field within Ω^- and, when the volume of Ω^- changes, no artificial pressure is generated within Ω^- at any time.

As mentioned above, the fluid equations need stabilizing terms for dominating convection and equal order interpolation as used in the following (equal order bi-quadratic). Note that we do not employ any stabilization terms on the Lagrange multiplier expression $(\boldsymbol{v}, \boldsymbol{\lambda})_{\Gamma^+}$.

3.4. Fluid discretization in space

3.4.1. Velocity and stress discontinuity across the fluid–structure interface

As should be clear by now, in the proposed fixed grid scheme, the fluid–structure interface is generally not aligned with fluid element edges. Consequently, we need to find a way to represent a jump in the primary variables, namely the velocity and pressure. Furthermore, also the derivatives have to be discontinuous, since the stressfield is discontinuous as well.

The eXtended Finite Element Method has been proposed [2,32] to represent structural material cracks as an example for such discontinuities. Here, the finite element shape functions are extended or enriched by using additional degrees of freedom combined with known solution or special enrichment functions. Applied to the velocity field, an enriched velocity approximation can be defined as

$$\boldsymbol{u}^{\mathrm{h}}(\boldsymbol{x}, t) = \sum_I N_I(\boldsymbol{x})(\tilde{\boldsymbol{u}}_I + \psi(\boldsymbol{x}, t)\hat{\boldsymbol{u}}_I). \tag{51}$$

Here, $\tilde{\boldsymbol{u}}_I$ represent the standard nodal degrees of freedom at node I, while additional degrees of freedom $\hat{\boldsymbol{u}}_I$ multiplied by a properly chosen enrichment function $\psi(\boldsymbol{x}, t)$ are used to enhance the solution.

The choice of the enrichment function depends on the character of the interface conditions. For our interface problem, we have a jump from the physical behavior in Ω^+ to basically nothing or zero velocity and pressure in Ω^-. Likewise, the viscous stress resulting from velocity derivatives are only present in the physical flow field, whereas in Ω^- they are zero as no flow occurs. Hence, a jump-like function, also allowing different gradients on both sides of the jump discontinuity, would properly describe the character of the interface.

Hence, for our purpose the enrichment function is defined as a step function $H(\boldsymbol{x},t)$

$$\psi(\boldsymbol{x}, t) = H(\boldsymbol{x}, t) = \begin{cases} +1 & \forall \boldsymbol{x} \in \Omega^+, \\ 0 & \forall \boldsymbol{x} \in \Omega^-. \end{cases} \tag{52}$$

In a similar situation, where a hole or void exists inside a continuum, already Daux et al. [10] introduced such a modified Heaviside function.

With the help of this Heaviside functions, most nodes and elements inside the hole can be removed resulting in savings in computation time. More important, it provides a convenient way of embedding an arbitrary jump inside the approximation functions. This jump goes from a finite boundary value in Ω^+ to zero in the fictitious domain Ω^-.

Along Γ^{i}, both velocity and pressure are discontinuous and enriched with H. The complete discretization for trial and test functions with equal order Ansatz functions for velocity and pressure are given as

$$\boldsymbol{u}^{\mathrm{h},n+1}(\boldsymbol{x}) = \sum_I N_I(\boldsymbol{x})(\tilde{\boldsymbol{u}}_I^{n+1} + H(\boldsymbol{x}, t^{n+1})\hat{\boldsymbol{u}}_I^{n+1}), \tag{53}$$

$$\boldsymbol{v}^{\mathrm{h}}(\boldsymbol{x}) = \sum_I N_I(\boldsymbol{x})(\tilde{\boldsymbol{v}}_I + H(\boldsymbol{x}, t^{n+1})\hat{\boldsymbol{v}}_I) \tag{54}$$

and

$$p^{\mathrm{h},n+1}(\boldsymbol{x}) = \sum_I N_I(\boldsymbol{x})(\tilde{p}_I^{n+1} + H(\boldsymbol{x}, t^{n+1})\hat{p}_I^{n+1}), \tag{55}$$

$$q^{\mathrm{h}}(\boldsymbol{x}) = \sum_I N_I(\boldsymbol{x})(\tilde{q}_I + H(\boldsymbol{x}, t^{n+1})\hat{q}_I). \tag{56}$$

The superscript 'h' indicates the discretized field function.

Away from the interface, spatial derivatives of enriched shape functions with respect to the spatial direction i are done using the product rule as

$$(N_I(\boldsymbol{x})H(\boldsymbol{x},t))_{,i} = N_{I,i}(\boldsymbol{x})H(\boldsymbol{x},t) + N_I(\boldsymbol{x})H_{,i}(\boldsymbol{x},t). \tag{57}$$

Since H is a constant function, the derivative of an enriched shape function is simply the derivative of the normal shape function multiplied by the step function H.

Across the interface, such derivatives would result in Dirac functions, which can be identified as traction jumps. These jumps are already accounted for by the traction vector $\boldsymbol{\lambda}$ along Γ^{i} representing the traction jump from Ω^+ to Ω^- in Eq. (50).

Fig. 4 shows enriched shape functions of a bi-linear 4 node element. Higher order shape functions, *e.g.* for the quadratic 9-node fluid element as used in the examples (see Section 6), are constructed with no additional effort making this approach capable for consistent low and high order finite element approximations.

Even several interfaces within one fluid element cause no problems. This feature allows thin structures to be treated within an FSI approach on 'large' fluid elements. If more than one interface crosses one fluid element, simply more enrichments can be used, using one enrichment for each interface. The additional unknowns $\hat{\boldsymbol{u}}_I^{\mathbf{1}}, \hat{\boldsymbol{u}}_I^{\mathbf{2}}, \ldots$ and enrichment functions $H^{\mathbf{1}}, H^{\mathbf{2}}, \ldots$ are summed as

$$\boldsymbol{u}^{\mathrm{h}}(\boldsymbol{x}) = \sum_I N_I(\boldsymbol{x})(\tilde{\boldsymbol{u}}_I + H^{\mathbf{1}}(\boldsymbol{x})\hat{\boldsymbol{u}}_I^{\mathbf{1}} + H^{\mathbf{2}}(\boldsymbol{x})\hat{\boldsymbol{u}}_I^{\mathbf{2}} + \cdots), \tag{58}$$

with the time dependence omitted for brevity. From an implementation point of view, we will refer to the standard degrees of freedom $\tilde{\boldsymbol{u}}$ also as the zeroth enrichment ($\psi^{\mathbf{0}} = 1$) as it is a set of nodal unknowns as any of the additional enrichment functions.

As time evolves and the interface moves, the enriched shape functions $N_I(\boldsymbol{x})\psi(\boldsymbol{x},t)$ at n and $n+1$ are generally different near the interface. However, within the XFEM context, the mesh topology does not change. Instead, the nodal unknowns are represented with varying shape functions, which becomes clear, when the weak form is diecretized in time first. Consequently, new enrichments can be initialized and removed without any 'mapping' between different meshes. A variation of such an update can be found in Réthoré et al. [37], a detailed treatment and analysis of this step will be topic of an upcoming paper.

3.4.2. Interface discretization

Along the interface Γ^{i}, the Lagrange multiplier field and the corresponding test functions are discretized as

$$\boldsymbol{\lambda}^{\mathrm{h}} = \sum_I N_I^{\mathrm{i}}\boldsymbol{\lambda}_I \quad \text{and} \quad \delta\boldsymbol{\lambda}^{\mathrm{h}} = \sum_I N_I^{\mathrm{i}}\delta\boldsymbol{\lambda}_I. \tag{59}$$

The choice of appropriate shape functions N_I^{i} can not be made without consideration of the underlying fluid discretization. Inappropriate choices can lead to oscillations or locking due to violation of the inf–sup condition. A recent discussion of applying Dirichlet boundary conditions in the context of XFEM can be found in [31]. For the implementation used in this paper, we used bi-quadratic ansatz functions for fluid velocity and pressure N_I and linear ansatz function for N_I^{i}, where no oscillation and locking was observed. The construction of the interface mesh is illustrated in Fig. 5.

The same shape functions N_I^{i} are also used to discretize the interface velocities and displacements

$$\boldsymbol{u}^{\mathrm{i,h}} = \sum_I N_I^{\mathrm{i}}\boldsymbol{u}_I^{\mathrm{i}}, \tag{60a}$$

$$\boldsymbol{d}^{\mathrm{i,h}} = \sum_I N_I^{\mathrm{i}}\delta\boldsymbol{d}_I^{\mathrm{i}}. \tag{60b}$$

3.4.3. Numerical integration of domain integrals

Elements divided by discontinuities are subdivided into subdomains using a constrained Delaunay algorithm and integration is performed over subdomains [32]. This integrates the piecewise bi-quadratic functions exact, but requires higher programming effort than alternative integration schemes.

3.5. Enrichment strategies

Along the structural surface we distinguish between two possible scenarios: In the first scenario, we have a relatively thick structure such that only one interface intersects a fluid element as depicted in Fig. 5. Here, all nodes belonging to an intersected element are enriched. All remaining nodes in Ω^+ use the standard degrees of freedom, while

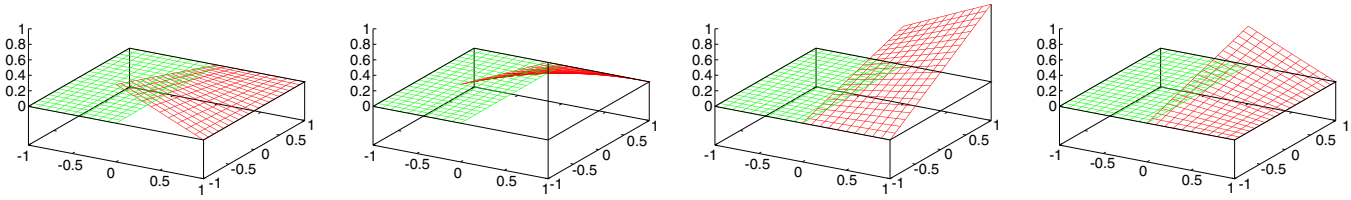

(a) $N_1(\boldsymbol{\xi})H(\boldsymbol{\xi},t)$ (b) $N_2(\boldsymbol{\xi})H(\boldsymbol{\xi},t)$ (c) $N_3(\boldsymbol{\xi})H(\boldsymbol{\xi},t)$ (d) $N_4(\boldsymbol{\xi})H(\boldsymbol{\xi},t)$

Fig. 4. Enriched shape functions for the 4 corner-nodes of a bi-linear element.

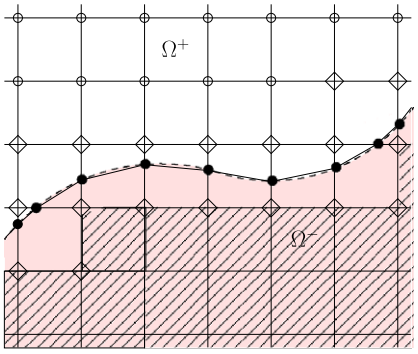

Fig. 5. Shown are the standard degrees of freedom (○) with the additional degrees of freedom (◊) needed for the jump enrichment. The striped elements are deactivated. The Lagrange multiplier nodes (•) are constructed on intersection between the interface and fluid element edges.

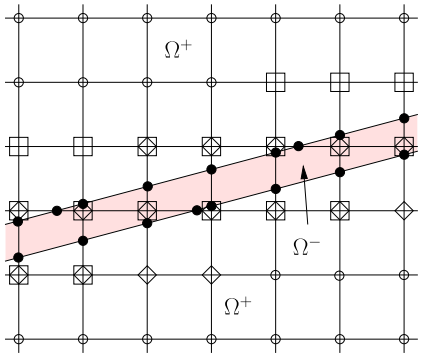

Fig. 6. For thin structures, two overlapping enrichments (◊ and □) represent the discontinuity, while away from the surface, standard degrees of freedom (○) are used. Lagrange multiplier meshes (•) are constructed on each side as usual.

the remaining nodes in Ω^- carry no degrees of freedom at all.

Within Ω^-, as stated before, both velocity and pressure will remain zero at all times, since no forces apply to its boundaries or its interior. This fact has an advantageous effect on the necessary degrees of freedom along the interface. In an intersected element in Ω^- the velocity is summed up as

$$\boldsymbol{u}^{\mathrm{h}}(\boldsymbol{x},t) = \boldsymbol{0} = \sum_I N_I(\boldsymbol{x})(\tilde{\boldsymbol{u}}_I(t) + 0\hat{\boldsymbol{u}}_I(t)) \quad \forall \boldsymbol{x} \in \Omega^-. \tag{61}$$

Consequently, the standard degree of freedom $\tilde{\boldsymbol{u}}$ have to be zero, since the approximated velocity $\boldsymbol{u}^{\mathrm{h}}(\boldsymbol{x},t)$ has to be zero within Ω^-. This allows to remove these degrees of freedom from intersected elements as shown in Fig. 5. In addition, all nodal velocities within Ω^- away from the surface will evaluate to zero and we can safely remove these interior elements. Consequently, we only have to integrate full elements in Ω^+ and subelements that are in Ω^+. Approaches, where integration is performed only on parts of an element to account for discontinuities can also be found in [19,39].

When dealing with thin structures more than one enrichment is necessary. This can be applied with ease as shown in Eq. (58). The enrichment for a structure as depicted in Fig. 6 consists of 2 overlapping jump enrichments using the step function Eq. (52). Again, integrating within Ω^- has to result in $\boldsymbol{u}^{\mathrm{h}} = \boldsymbol{0}$, consequently, all jump enrichments are zero within Ω^-. Hence, standard degrees of freedom of intersected elements have to be zero and can be removed. Results for a computation involving such thin structures are given in Section 6.2.

3.6. Solution of the fluid equations

The complete fluid–interface system including the Lagrange multiplier formulation becomes

$$\begin{bmatrix} \mathbf{A}_{uu} & \mathbf{A}_{up} & -\Delta t\theta \mathbf{M}_\lambda^{\mathrm{T}} \\ \mathbf{A}_{pu} & \mathbf{A}_{pp} & \mathbf{0} \\ -\Delta t\theta \mathbf{M}_\lambda & \mathbf{0} & \mathbf{0} \end{bmatrix} \begin{bmatrix} \mathbf{u} \\ \mathbf{p} \\ \boldsymbol{\lambda} \end{bmatrix} = \begin{bmatrix} \mathbf{f}^{\mathrm{rhs}} \\ \mathbf{0} \\ -\Delta t\theta \mathbf{D}_\lambda \bar{\mathbf{u}}^{\mathrm{i}} \end{bmatrix}, \tag{62}$$

where

$$\mathbf{D}_\lambda: \quad D_{LIij} = \int_{\Gamma^+} N_I^{\mathrm{i}} N_J^{\mathrm{i}} \,\mathrm{d}\boldsymbol{x} \delta_{ij} \tag{63}$$

and

$$\mathbf{M}_\lambda: \quad M_{KLij} = \int_{\Gamma^+} N_K^{\mathrm{i}} N_L^{\mathrm{f}} \,\mathrm{d}\boldsymbol{x} \delta_{ij}, \tag{64}$$

with δ_{ij} being the Kronecker-δ, *i.e.* $\delta_{ij} = 1$ if $i = j$, else 0.

The submatrices $\mathbf{A}_{uu}$, $\mathbf{A}_{up}$, $\mathbf{A}_{pu}$ and $\mathbf{A}_{pp}$ denote the standard matrices arising in stabilized FE formulations of the Navier–Stokes equation.

The presented approach allows to decouple the physical domain from the fictitious domain Ω^- and weakly apply Dirichlet boundary conditions along the interface. It can now be used in an coupled FSI approach presented in Section 5.

4. Structure–interface coupling

In the previous section, we constructed the discretization of the interface based on the fluid element edges. The resulting interface mesh generally does not match the surface discretization of the structure. Therefore, we require a method that can handle the coupling of non-matching surface grids. The problem of non-matching grids often occurs in the process of domain decomposition, hence, extensive research has been undertaken. For the problem at hand, we adopt the Mortar methods for non-matching grids [6,7] and [46].

4.1. Setup of Mortar coupling

The interface condition in Eq. (31) is formulated in terms of velocities, however it implies that not only are the velocities equal at all times but also the positions or displacements of the interface and structural surface. Hence, instead of Eq. (31), we can state

$$\boldsymbol{d}^{\mathrm{s}} = \boldsymbol{d}^{\mathrm{i}} \quad \forall \boldsymbol{x} \in \Gamma^{\mathrm{i}}. \tag{65}$$

In the Mortar method, the kinematic matching condition (65) is enforced weakly by using a Lagrange multiplier field $\boldsymbol{\mu}$, which can be identified with the surface traction $\boldsymbol{\mu}$ in Eq. (33). The setup for the structure–interface coupling is depicted in Fig. 7.

The weak form of the structural momentum equation from Eq. (26) including the interface condition in Eq. (65) reads as

$$\delta W^{\mathrm{s}} = 0 = (\delta \boldsymbol{d}^{\mathrm{s}}, \rho^{\mathrm{s}} \ddot{\boldsymbol{d}}^{\mathrm{s}})_{\Omega^{\mathrm{s}}} - (\delta \boldsymbol{d}^{\mathrm{s}}, \nabla \cdot \boldsymbol{\sigma}^{\mathrm{s}})_{\Omega^{\mathrm{s}}} + (\delta \boldsymbol{\mu}, \boldsymbol{d}^{\mathrm{s}} - \boldsymbol{d}^{\mathrm{i}})_{\Gamma^{\mathrm{i}}}. \tag{66}$$

Integration by parts of the stress term gives

$$-(\delta \boldsymbol{d}^{\mathrm{s}}, \nabla \cdot \boldsymbol{\sigma}^{\mathrm{s}})_{\Omega^{\mathrm{s}}} = -(\delta \boldsymbol{d}^{\mathrm{s}}, \boldsymbol{\sigma}^{\mathrm{s}} \cdot \boldsymbol{n}^{\mathrm{s}})_{\Gamma^{\mathrm{s}}} + (\nabla \cdot \delta \boldsymbol{d}^{\mathrm{s}}, \boldsymbol{\sigma}^{\mathrm{s}})_{\Omega^{\mathrm{s}}}. \tag{67}$$

For Dirichlet boundary conditions, the surface integral vanishes due to the vanishing test function. Neumann conditions are applied by letting $\boldsymbol{\sigma}^{\mathrm{s}} \cdot \boldsymbol{n}^{\mathrm{s}} = \bar{\boldsymbol{h}}^{\mathrm{s}}$. Implementation of the Neumann conditions is straightforward and will not be discussed further for brevity. The resulting weak form is

$$(\delta \boldsymbol{d}^{\mathrm{s}}, \rho^{\mathrm{s}} \ddot{\boldsymbol{d}}^{\mathrm{s}})_{\Omega^{\mathrm{s}}} + (\nabla \delta \boldsymbol{d}^{\mathrm{s}}, \boldsymbol{\sigma}^{\mathrm{s}})_{\Omega^{\mathrm{s}}} - (\delta \boldsymbol{d}^{\mathrm{s}}, \boldsymbol{\mu})_{\Gamma^{\mathrm{i}}} - (\delta \boldsymbol{\mu}, \boldsymbol{d}^{\mathrm{s}} - \boldsymbol{d}^{\mathrm{i}})_{\Gamma^{\mathrm{i}}} = 0. \tag{68}$$

4.2. Spatial discretization

The discretization of the structural displacement is done using shape function N_I^{s}

$$\boldsymbol{d}^{\mathrm{s,h}} = \sum_I N_I^{\mathrm{s}} \mathbf{d}_I^{\mathrm{s}} \quad \text{and} \quad \delta \boldsymbol{d}^{\mathrm{s,h}} = \sum_I N_I^{\mathrm{s}} \delta \mathbf{d}_I^{\mathrm{s}}. \tag{69}$$

In the Mortar method, the Lagrange multiplier is discretized with the shape functions and node set of the slave side. Let the interface Γ^{i} be the slave side and the structural surface the master side in the Mortar problem. The interface has already been discretized using shape functions N_I^{i} from Eq. (60). Consequently, trial and test functions of the Lagrange multiplier field are discretized as

$$\boldsymbol{\mu}^{\mathrm{h}} = \sum_I N_I^{\mathrm{i}} \boldsymbol{\mu}_I \quad \text{and} \quad \delta \boldsymbol{\mu}^{\mathrm{h}} = \sum_I N_I^{\mathrm{i}} \delta \boldsymbol{\mu}_I. \tag{70}$$

Furthermore, the interface may be curved and surface elements do not necessarily coincide with the interface elements. Consequently, we need a projection $\mathscr{P}^{\mathrm{s}}$ [46] to integrate the weak form.

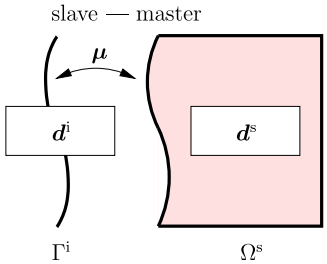

Fig. 7. Mortar coupling between structural surface and interface.

$$\delta W^{\mathrm{s}} = 0 = \int_{\Gamma^{\mathrm{i}}} \delta \boldsymbol{\mu}^{\mathrm{h}} (\mathscr{P}^{\mathrm{s}} \boldsymbol{d}^{\mathrm{s,h}} - \boldsymbol{d}^{\mathrm{i,h}}) \, \mathrm{d}\boldsymbol{x}. \tag{71}$$

The virtual work δW^{s} done by the virtual force $\delta \boldsymbol{\mu}^{\mathrm{h}}$ allows to define two coupling matrices $\mathbf{M}_\mu$ and $\mathbf{D}_\mu$ as

$$0 = \delta \mu_{Ji} \left[\underbrace{\int_{\Gamma^{\mathrm{i}}} N_I^{\mathrm{i}} \mathscr{P}^{\mathrm{s}} N_J^{\mathrm{s}} \, \mathrm{d}\boldsymbol{x}}_{\mathbf{M}_\mu} d_{Ji}^{\mathrm{s}} - \underbrace{\int_{\Gamma^{\mathrm{i}}} N_I^{\mathrm{i}} N_K^{\mathrm{i}} \, \mathrm{d}\boldsymbol{x}}_{\mathbf{D}_\mu} d_{Ki}^{\mathrm{i}} \right]. \tag{72}$$

With the help of this system of equations in Eq. (72), it is possible to calculate the interface position based on the structural surface position

$$\mathbf{d}^{\mathrm{i}} = \mathbf{D}_\mu^{-1} \mathbf{M}_\mu \mathbf{d}^{\mathrm{s}}. \tag{73}$$

The corresponding Neumann condition along Γ^{i} can be derived from the integral $(\delta \boldsymbol{d}^{\mathrm{s}}, \boldsymbol{\mu})_{\Gamma^{\mathrm{i}}}$. The Lagrange multiplier field $\boldsymbol{\mu}$ is recognized as the surface traction field acting on the structural surface. Writing this integral in its discretized form and again using above projection we get

$$(\delta \boldsymbol{d}^{\mathrm{s,h}}, \boldsymbol{\mu}^{\mathrm{h}})_{\Gamma^{\mathrm{i}}} = \int_{\Gamma^{\mathrm{i}}} \mathscr{P}^{\mathrm{s}} N_I^{\mathrm{s}} \delta d_{Ii}^{\mathrm{s}} N_J^{\mathrm{i}} \mu_{Ji} \, \mathrm{d}\boldsymbol{x}. \tag{74}$$

Now the Neumann force vector can simply be written as

$$f_{Ii}^{\mathrm{s,fsi}} = \underbrace{\int_{\Gamma^{\mathrm{i}}} \mathscr{P}^{\mathrm{s}} N_I^{\mathrm{s}} N_J^{\mathrm{i}} \, \mathrm{d}\boldsymbol{x}}_{\mathbf{M}_\mu^{\mathrm{T}}} \mu_{Ji} \tag{75}$$

or, in matrix notation,

$$\mathbf{f}^{\mathrm{s,fsi}} = \mathbf{M}_\mu^{\mathrm{T}} \boldsymbol{\mu}. \tag{76}$$

4.3. Time discretization

For structural time integration, a β-Newmark scheme [5,21] is employed with parameters set to $\beta = 0.25$ and $\gamma = 0.5$ making it an implicit time integration scheme

$$\boldsymbol{a}^{n+1} = \frac{1}{\beta \Delta t^2} (\boldsymbol{d}^{n+1} - \boldsymbol{d}^n) - \frac{1}{\beta \Delta t} \boldsymbol{v}^n - \frac{1 - 2\beta}{2\beta} \boldsymbol{a}^n, \tag{77}$$

$$\boldsymbol{v}^{n+1} = \boldsymbol{v}^n + \gamma \Delta t \boldsymbol{a}^{n+1} + (1 - \gamma) \Delta t \boldsymbol{a}^n. \tag{78}$$

With the definition of an effective tangent stiffness $\mathbf{A}_d$ as

$$\mathbf{A}_d = \frac{1}{\beta \Delta t^2} \mathbf{M} - \mathbf{K} \tag{79}$$

and an effective force $\mathbf{f}^{\mathrm{dyn}}$ representing terms from the old time step as

$$\mathbf{f}^{\mathrm{dyn}} = -\frac{1}{\Delta t^2} \mathbf{M} \mathbf{d}^n + \frac{1 - 2\beta}{2\beta} \mathbf{M} \ddot{\mathbf{d}}^n \tag{80}$$

the fully discretized structural equations are given as

$$\begin{bmatrix} \mathbf{0} & -\mathbf{M}_\mu \\ -\mathbf{M}_\mu^{\mathrm{T}} & \mathbf{A}_d \end{bmatrix} \begin{bmatrix} \boldsymbol{\mu} \\ \mathbf{d}^{\mathrm{s}} \end{bmatrix} = \begin{bmatrix} -\mathbf{D}_\mu \bar{\mathbf{d}}^{\mathrm{i}} \\ \mathbf{f}^{\mathrm{dyn}} \end{bmatrix}. \tag{81}$$

Here, the interface displacement $\bar{\mathbf{d}}^{\mathrm{i}}$ is assumed to be known, which will change, when we use Eq. (81) in the complete fluid–structure system.

5. Partitioned fluid–structure coupling

5.1. Combined fluid–structure system

In this section, we combine both fields in one coupled system. The fully coupled system using three distinct fields Ω, Ω^{s} and Γ^{i} is shown in Fig. 8. The structure domain is coupled via a Mortar formulation to the interface. On the other side, the fixed grid fluid domain with the projected interface (dashed line) couples via a second Lagrange multiplier field to the same interface. The interface is the slave side for both couplings – the fluid–interface coupling and the structure–interface coupling.

Before the coupled problem can be posed, the interface velocity $\boldsymbol{u}^{\mathrm{i}}$ has to be discretized in time, since displacement $\boldsymbol{d}^{\mathrm{i}}$ and velocity $\boldsymbol{u}^{\mathrm{i}}$ of the surface are connected by the simple differential equation $\dot{\boldsymbol{d}}^{\mathrm{i}} = \boldsymbol{u}^{\mathrm{i}}$.

For simplicity, we again choose the one-step-θ method for the interface movement such that the time-discrete form of $\dot{\boldsymbol{d}}^{\mathrm{i}} = \boldsymbol{u}^{\mathrm{i}}$ becomes

$$\frac{\boldsymbol{d}^{\mathrm{i},n+1} - \boldsymbol{d}^{\mathrm{i},n}}{\Delta t} = \theta^{\mathrm{i}} \boldsymbol{u}^{\mathrm{i},n+1} + (1-\theta^{\mathrm{i}}) \boldsymbol{u}^{\mathrm{i},n}. \tag{82}$$

With the help of Eq. (82), it is possible to prescribe the interface position instead of the interface velocity using the given interface displacement $\bar{\boldsymbol{d}}^{\mathrm{i},n+1}$ and a predictor $\boldsymbol{d}^{\mathrm{i,pred}}$

$$\boldsymbol{u}^{\mathrm{i},n+1} = \frac{1}{\Delta t \theta^{\mathrm{i}}} (\bar{\boldsymbol{d}}^{\mathrm{i},n+1} - \boldsymbol{d}^{\mathrm{i,pred}}), \tag{83}$$

with the predictor defined as

$$\boldsymbol{d}^{\mathrm{i,pred}} = \Delta t (1-\theta^{\mathrm{i}}) \boldsymbol{u}^{\mathrm{i},n} + \boldsymbol{d}^{\mathrm{i},n}. \tag{84}$$

For second order accuracy, θ^{i} has to be chosen as $\theta^{\mathrm{i}} = 0.5$ resulting in the second order trapezoidal rule, which is also consistent with the structural time discretization. However, it is noted in [14] that the trapezoidal rule might lead to oscillations, since no damping is included in the trapezoidal rule. For the presented calculations, $\theta^{\mathrm{i}} = 0.5$ has been used.

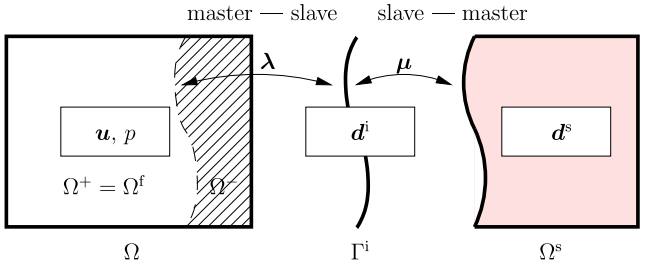

Fig. 8. Coupled problem with 3 fields, along with variables living on each domain and the Lagrange multiplier fields.

Using Eqs. (83) and (84), the bottom line of the fluid system of Eq. (62) would become

$$-\Delta t \theta^{\mathrm{i}} \mathbf{M}_{\lambda} \mathbf{u} = -\mathbf{D}_{\lambda} (\bar{\boldsymbol{d}}^{\mathrm{i},n+1} - \boldsymbol{d}^{\mathrm{i,pred}}), \tag{85}$$

where the interface displacement of the new time step is prescribed.

A second change to the fluid system lies in the construction of the interface. In the fluid derivation it was stated that the interface discretization is derived from the intersection points of a smooth interface crossing the fluid element edges. After structural discretization, only the (Lagrangian) structural surface mesh prescribes, where the surface is located. Consequently, we now construct the interface from the intersection of structural surface edges with fluid element edges as shown in Fig. 9.

5.2. Monolithic system

So far, we have derived the discrete system for the single fluid and structural field, which are constrained towards the interface movement. The second condition to be fulfilled is the traction balance along the interface (34). This equality must hold also in the discrete system. The discrete equivalent expression for Eq. (34) is

$$\boldsymbol{\lambda} + \boldsymbol{\mu} = 0. \tag{86}$$

The three field variables $\boldsymbol{\lambda}$, $\boldsymbol{d}^{\mathrm{i}}$ and $\boldsymbol{\mu}$ use the same number of nodes and the same approximation functions N_I^{i} (see also Fig. 9). Consequently, matrix $\mathbf{D}_{\mu}$ is identical to $\mathbf{D}_{\lambda}$. Therefore, the above equation can be extended as

$$\mathbf{D}_{\lambda}^{\mathrm{T}} \boldsymbol{\lambda} + \mathbf{D}_{\mu}^{\mathrm{T}} \boldsymbol{\mu} = 0, \tag{87}$$

which is true since $\mathbf{D}_{\lambda}^{\mathrm{T}} = \mathbf{D}_{\mu}^{\mathrm{T}}$ because of the chosen interface discretization for the Lagrange multipliers.

This allows to pose the complete coupled discrete system as

$$\begin{bmatrix} \mathbf{A}_{uu} & \mathbf{A}_{up} & -\Delta t \theta \mathbf{M}_{\lambda}^{\mathrm{T}} & \mathbf{0} & \mathbf{0} & \mathbf{0} \\ \mathbf{A}_{pu} & \mathbf{A}_{pp} & \mathbf{0} & \mathbf{0} & \mathbf{0} & \mathbf{0} \\ -\Delta t \theta^{\mathrm{i}} \mathbf{M}_{\lambda} & \mathbf{0} & \mathbf{0} & \mathbf{D}_{\lambda} & \mathbf{0} & \mathbf{0} \\ \mathbf{0} & \mathbf{0} & \mathbf{D}_{\lambda}^{\mathrm{T}} & \mathbf{0} & \mathbf{D}_{\mu}^{\mathrm{T}} & \mathbf{0} \\ \mathbf{0} & \mathbf{0} & \mathbf{0} & \mathbf{D}_{\mu} & \mathbf{0} & -\mathbf{M}_{\mu} \\ \mathbf{0} & \mathbf{0} & \mathbf{0} & \mathbf{0} & -\mathbf{M}_{\mu}^{\mathrm{T}} & \mathbf{A}_{d} \end{bmatrix} \begin{bmatrix} \mathbf{u} \\ \mathbf{p} \\ \boldsymbol{\lambda} \\ \mathbf{d}^{\mathrm{i}} \\ \boldsymbol{\mu} \\ \mathbf{d}^{\mathrm{s}} \end{bmatrix} = \begin{bmatrix} \mathbf{f}^{\mathrm{rhs}} \\ \mathbf{0} \\ \mathbf{D}_{\lambda} \mathbf{d}^{\mathrm{i,pred}} \\ \mathbf{0} \\ \mathbf{0} \\ \mathbf{f}^{\mathrm{dyn}} \end{bmatrix}. \tag{88}$$

The interface displacement solely serves as an intermediate field and is part of the solution, if this system would be solved as is. However, we prefer to partition the system as shown in the following.

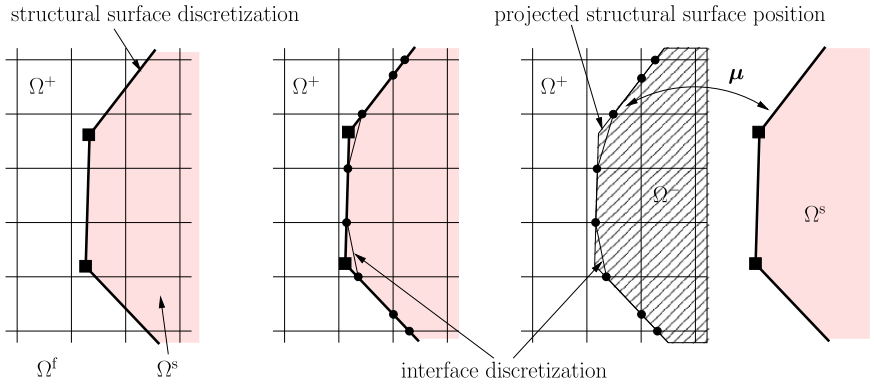

Fig. 9. Interface construction using the discrete structural surface: On the left, the structural surface and the fluid mesh is shown. Lagrange nodes (•) are located on the intersection between structural surface and fluid edges. The resulting interface mesh is used for both Mortar fields $\boldsymbol{\lambda}$ and $\boldsymbol{\mu}$ and the interface displacement $\mathbf{d}^{\mathrm{i}}$. The projected structural surface position is used for creation of integration triangles (triangles not shown). The mortar coupling takes place between structural surface and the nonconforming interface mesh.

5.3. Iterative staggered strong coupling scheme

The algorithmic implementation of the coupled problem of fluid–structure interaction is based on a field-wise partitioned solution approach. For that purpose, we separate the monolithic problem in Eq. (88) by eliminating the Lagrange multiplier field $\boldsymbol{\mu}$ and replacing it with an iterative approach.

The wet structural surface is the natural interface or coupling surface Γ^{i}. Complete kinematic and dynamic continuity at Γ^{i} would ensure conservation of mass, momentum and energy at the interface. The boundary conditions in this Dirichlet–Neumann sub-structuring scheme are chosen such that forces generated from the fluid pressure and viscous friction are exerted on the structural interface as Neumann boundary conditions. Hence, the Neumann problem in the context of the interface–structure coupling can be summarized as

$$\mathbf{A}_d\mathbf{d} = \mathbf{f}^{\mathrm{dyn}} + \mathbf{f}^{\mathrm{s,fsi}}, \tag{89}$$

with the nodal force $\mathbf{f}^{\mathrm{s,fsi}}$ calculated from the Lagrange multiplier in Eq (75).

After mapping the structural displacement onto the interface Γ^{i} via Eq. (73), the interface velocity can be calculated using Eq. (83) and is subsequently used as a Dirichlet condition for the fluid field. The fluid field can then be solved using the fluid system of equations given in Eq. (62).

For the dynamic FSI problems involving incompressible fluid flow and lightweight structures considered here, we employ an iterative staggered scheme based on [29,30,44], where each field is solved implicitly and an iterative procedure over the fields ensures convergence for the interface conditions at the new time step level $n+1$. In [15] it has been shown that such strong coupling schemes are necessary for such cases. The complete procedure is summarized in Algorithm 1. As proposed in [30,44], we use Aitken's acceleration scheme for vector sequences [23] to obtain the relaxation parameter ω_i.

Algorithm 1. Iterative Fluid–Structure Coupling

for each new time step $n+1$
  Compute an explicit predictor of the structural interface displacement at the new time level $\mathbf{d}_0^{\mathrm{i},n+1}$
  for each FSI iteration i
    establish interface mesh
    compute $\mathbf{D}_\mu$,$\mathbf{M}_\mu$ Eq. (72)
    Structure → Fluid: Transfer interface displacement $\mathbf{d}_{i+1}^{\mathrm{i},n+1} = \mathbf{D}_\mu^{-1}\mathbf{M}_\mu\mathbf{d}_{i+1}^{\mathrm{s},n+1}$ Eq. (73)
    Compute interface velocity $\mathbf{u}_{i+1}^{\mathrm{i},n+1}$ from interface displacement Eq. (83)
    Fluid: Solve fluid equations to obtain $\mathbf{u}_{i+1}^{n+1}$, $\mathbf{p}_{i+1}^{n+1}$ and fluid interface traction $\boldsymbol{\lambda}_{i+1}^{n+1}$ Eq. (62)
    Fluid → Structure: Transfer reaction force $\mathbf{f}_{i+1}^{\mathrm{s,fsi},n+1} = -\mathbf{M}_\mu^{\mathrm{T}}\boldsymbol{\lambda}_{i+1}^{n+1}$ Eq. (75)
    Structure: Solve for new displacements $\mathbf{d}_{i+1}^{\mathrm{s},n+1}$ Eq. (81)
    Check convergence
    if not converged
      Relax structural displacements along the surface $\mathbf{d}_{i+1}^{\mathrm{s},n+1} = \omega_i\mathbf{d}_{i+1}^{\mathrm{s},n+1} + (1-\omega_i)\mathbf{d}_i^{\mathrm{s},n+1}$
      Restart iteration with new interface position.
    end if
  for
end for

6. Numerical examples

In the following section, simulation results on fluid flow around elastic objects of varying stiffness are shown. The intention is to demonstrate the flexibility with respect to structural shapes that can be used in the simulation. Coarse meshes have been used to show essential features of the enrichment and to demonstrate that the decoupling works for arbitrary fluid mesh densities.

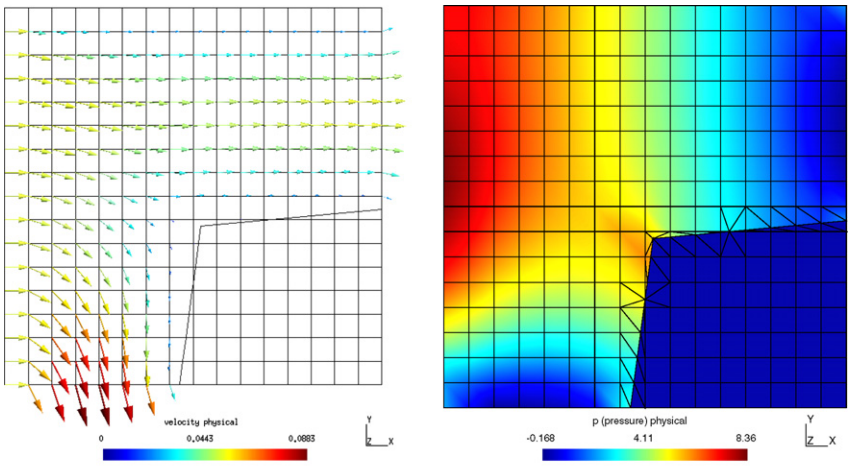

(a) Flow field (b) Pressure field

Fig. 10. Flow field around a stationary structure. The structure is located in the lower right corner. The inflow from the left boundary ($\boldsymbol{u} = (0.05, 0.0, 0.0)^{\mathrm{T}}$) and the wall boundary at the top are standard Dirichlet boundary conditions. The remaining boundaries are of Neumann (zero traction) type.

For postprocessing purpose of scalar views, the intersected elements are shown using the triangular integration subdomains. They solely serve to properly display the sharp interface in the postprocessing tool. Standard elements would display a smeared solution, because the postprocessor has no information about the enrichment functions. Fluid elements without an intersecting solid boundary are displayed as 9-node quadrilateral elements. All results are postprocessed using Gmsh [16].

6.1. Flow against a stationary wall

The first example, shown in Fig. 10, illustrates a flow around a structural corner. It can clearly be seen that there is no fluid flow within the structural domain in the lower right corner, although the interface is clearly not aligned with any fluid element boundary. The velocity along the fluid–structure interface is zero as prescribed using the Lagrange multipliers on the interface. It requires only 753 degrees of freedom (dof) compared to 1005 dof when all elements are calculated. This shows the principal advantage of removing the interior fluid elements and nodes to save calculation time and memory.

6.2. Flow around a thin structure

In the second example, different flow fields develop around a thin structure, which thickness is smaller than the fluid element size. On the left side, a horizontal parabolic inflow is applied, while on the right some constant diagonal inflow enters the domain. It can be clearly seen in Figs. 11a and b, how the pressure and the velocities of the flow right and left of the structure are completely decoupled from each other and the small fictitious fluid domain between them.

The three sets of enrichments for the pressure given by

$$p^{\mathrm{h}}(\boldsymbol{x}) = \sum_I N_I(\boldsymbol{x})\left(\tilde{p}_I + H^{\mathbf{1}}(\boldsymbol{x})\hat{p}_I^{\mathbf{1}} + H^{\mathbf{2}}(\boldsymbol{x})\hat{p}_I^{\mathbf{2}}\right) \tag{90}$$

are shown in Figs. 12a–c (see also Eq. (58)). The standard degrees of freedom, depicted in Fig. 12a occupy most of the domain. Near the surface the first and the second enrichment overlap each other (Figs. 12b and c). The sum of these enrichments gives the pressure field as displayed in Fig. 11b.[1]

6.3. Rotating cylinder

This example shows incompressible flows interacting with a rather soft, compressible (Poisson ratio $\nu = 0.0$) structure exhibiting large deformation. Through the appearing rotations of the structure it would cause some challenges to ALE-type methods. Therefore, already in such a simple setup it demonstrates potential applications of fixed grid methods. The setup is a unit square with Dirichlet boundary condition at the top and bottom of the square and 'do nothing' Neumann conditions along the right and left side producing a simple shear flow.

A 2d-cylinder representation is located in the center of the domain with the center node fixed. The viscous forces will enforce a rotation around its center. Additionally, the structure deforms due to the pressure acting on the structural surface.

The flow solution and the corresponding structural nodal forces are depicted in Fig. 13. From the fluid point of view, this problem becomes steady once the structure has reached the final shape as shown in the pictures. However, the structure keeps rotating, making this a transient problem after all. If the simulation is not stopped by the user, the rotation goes on indefinitely.

In contrast, methods using deforming fluid meshes would fail because of the excessive fluid mesh deformation.

[1] Note that displayed triangles are not part of the discretization and are only used for proper visualization of the results (and for numerical integration).

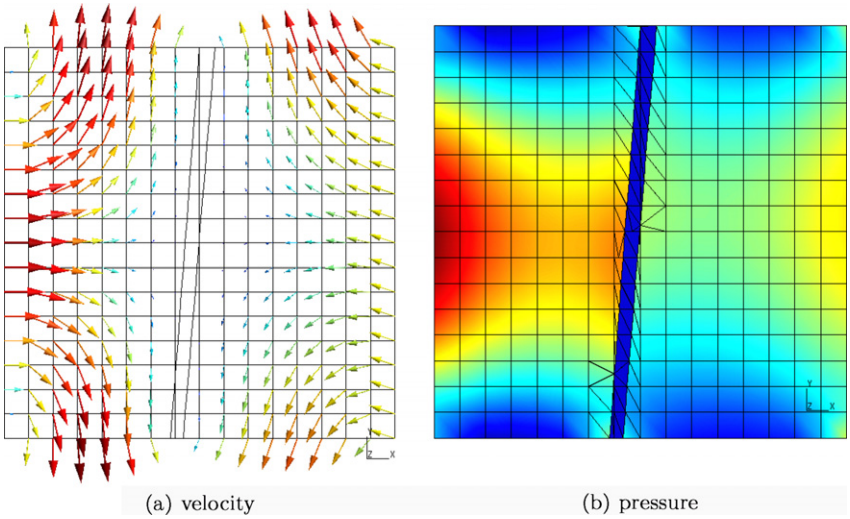

(a) velocity (b) pressure

Fig. 11. Flow field around a stationary thin structure. Note, that the thickness of the structure is less than the element size of the fluid. Now flow is observed within the structural domain and right and left flow field are completely decoupled. The integration triangles are only shown in the pressure field on the right.

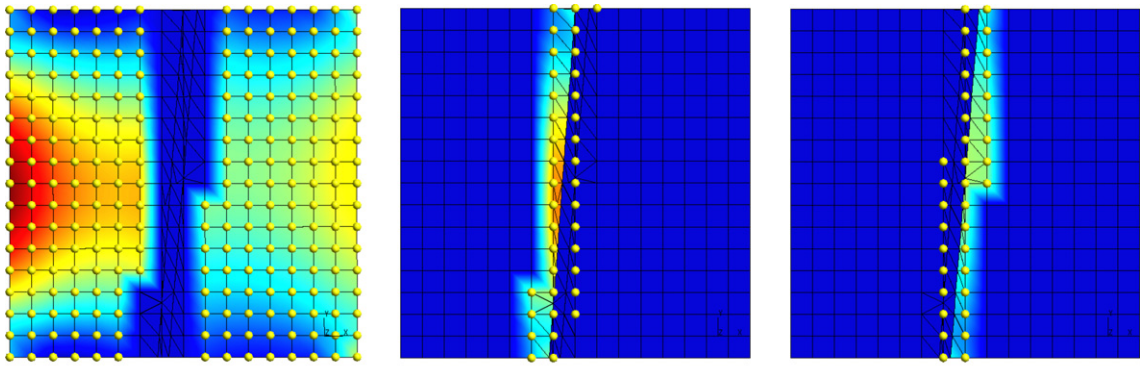

(a) zero-th enrichment: $\sum_I N_I(\boldsymbol{x})\bar{p}_I$ (b) first enrichment: $\sum_I N_I H^{\mathbf{1}}(\boldsymbol{x})\hat{p}_I^1$ (c) second enrichment: $\sum_I N_I H^{\mathbf{2}}(\boldsymbol{x})\hat{p}_I^2$

Fig. 12. Flow field around a stationary thin structure and enrichments used for the flow field around a stationary structure. The dots indicate the enriched nodes used for the particular enrichment. Summation of all enrichment terms results in the complete solution as shown in Fig. 11b.

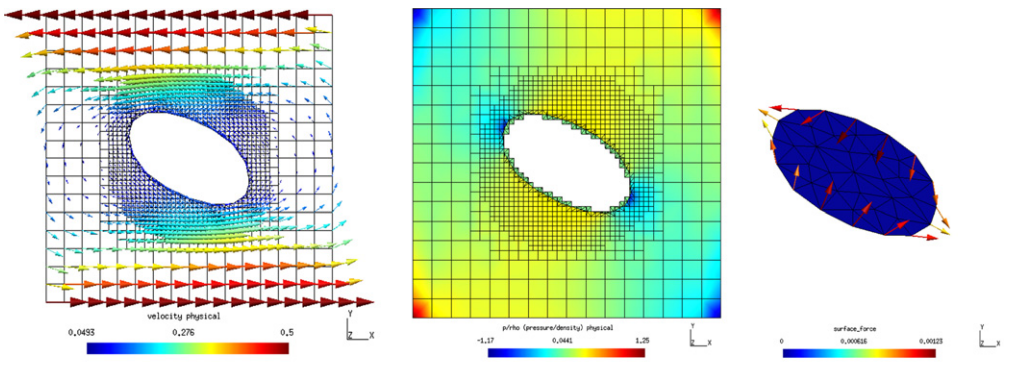

(a) velocity field $\mathbf{u}$ (b) pressure field $\mathbf{p}$ (c) surface nodal forces $\mathbf{f}^{\mathbf{s,fsi}}$

Fig. 13. Flow field around a flexible, rotating cylinder.

A qualitative comparison was performed with an ALE fluid field description using the same partitioned FSI algorithm. Depending on the mesh smoothing algorithm, convergence stopped after about 50–180° rotation angle.

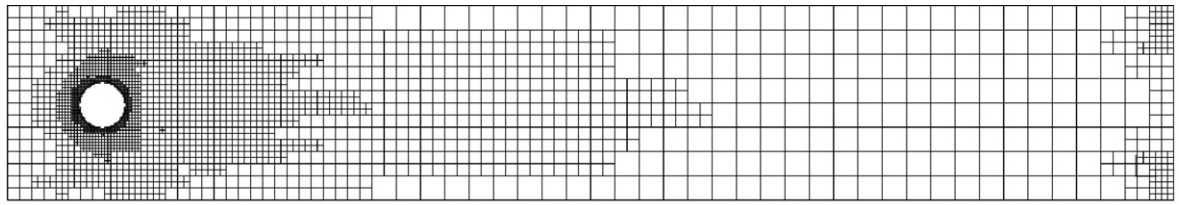

(a) Maximal refinement used in computation

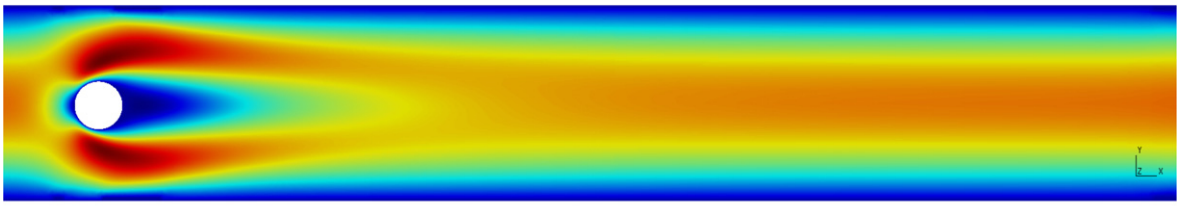

(b) x-component of the velocity field

Fig. 14. CFD benchmark: Finest mesh used to calculate lift and drag values on the cylinder. It consists of 284 Lagrange elements and 284 Lagrange nodes and 2740 quadratic 9-node fluid elements. Fig. 14 shows the x-component of the velocity field. The structure is not displayed.

6.4. Stationary flow around a cylinder

As a kind of benchmark problem and final example, we choose to compare the stationary flow around a cylinder, which is the first test case as defined in Schäfer and Turek [38] with their reference values. Since currently no good and well documented FSI-benchmarks are available we will use this example to quantitatively verify our approach.

To test not only the fluid solver but also the correct transfer of interface forces, we simulated the fixed cylinder by using the fully coupled, stationary FSI algorithm from Section 5.3 in conjunction with a very stiff structure fixed at three points away from the FSI surface.

The final setup can be seen in Fig. 14. The velocity component u_x of the fluid solution is shown over the whole fluid domain in Fig. 14 and near the interface in Fig. 15. Again note that the triangles in intersected elements are only for visualization and integration. Subdomains within the structural domain have been removed from the plot.

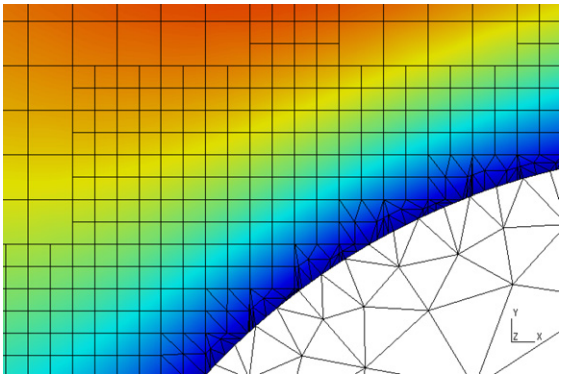

Fig. 15. x-Component of the velocity field near the interface. Again, note the integration triangles near the interface used for visualization and numerical integration.

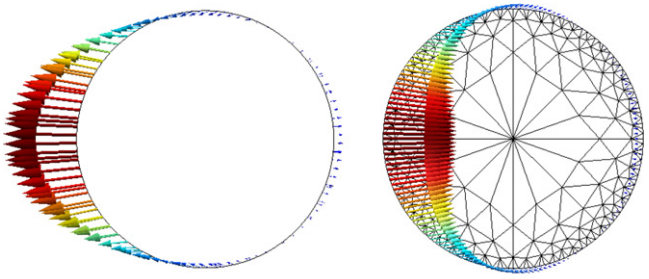

(a) Lagrange multiplier solution $\boldsymbol{\lambda}$ on Γ^{i} (b) Surface nodal forces $\mathbf{f}^{fsi}$

Fig. 16. Lagrange multiplier field on interface discretization and structural surface nodal forces on structural discretization.

Fig. 16 visually compares the solution of the Lagrange multiplier field $\boldsymbol{\lambda}$ with the projected nodal forces $\mathbf{f}^{fsi}$ on the structural surface nodes.

Fig. 14 shows the finest mesh that we used to study this problem. With this, we could already achieve very good agreement with the averaged results given in [38]. In particular, we calculated $c_L = 0.0054$ for the lift, $c_D = 5.5624$ for the drag and $\Delta p^f/\rho = 0.1172\ m^2/s^2$ for the normalized pressure difference.

The benchmark also clearly shows the potential gains in efficiency along with adaptive meshing when using fixed grid methods for the fluid domain, since uniform refinement is not a real option in complex fluid simulations.

7. Conclusion

Fixed grid methods for fluid–structure interaction are subject of a growing number of current research undertaken. The ultimate goal is to remove the burden of fluid mesh movement and, if deformation of the structure becomes excessive, re-meshing. For that purpose, we

worked out a list of minimal requirements that have to be fulfilled before fixed grid methods can match or surpass ALE based methods.

In an attempt to meet these requirements, we proposed a new XFEM based approach. Main improvements compared to most IB and DLM/FD methods are the complete removal of the fictitious domain and a sharp interface description. Physical and fictitious domains are completely decoupled and the fluid unknowns from within the fictitious domain could be removed from the fluid system of equation.

The use of a partitioned instead of a monolithic approach allows us to separate efforts on improving each field solution techniques. Due to the 3-field approach, the treatment of the structure is independent of any internals of the fluid XFEM discretization. From the structural point of view, the coupling exists solely between structural surface and the interface and can be independently improved on the latest advancements in the field of domain decomposition and Mortar methods. It will also simplify the subsequent development of an efficient, parallel XFEM fluid solver without modifying the structural solver.

With the basic framework described in this paper, various direction of research are possible. Further studies will focus on FSI coupling, on flow around sharp corners and a complete second order spatial discretization for fluid, structure and the interface required for accurate solutions of the FSI problems. Finally, a fast 3d-implementation using parallel algorithms is essential to simulate real-world applications.

Acknowledgements

The present study is supported by a grant of the 'Deutsche Forschungsgemeinschaft' (DFG) within the DFG's Research Unit 493 'FSI: Modelling, Simulation, and Optimization'. This support is gratefully acknowledged.

References

[1] F.P.T. Baaijens, A fictitious domain/mortar element method for fluid–structure interaction, Int. J. Numer. Methods Fluids 35 (7) (2001) 743–761.
[2] T. Belytschko, T. Black, Elastic crack growth in finite elements with minimal remeshing, Int. J. Numer. Methods Engrg. 45 (5) (1999) 601–620.
[3] T. Belytschko, J.M. Kennedy, Computer models for subassembly simulation, J. Nucl. Engrg. Des. 49 (1978) 17–38.
[4] T. Belytschko, J.M. Kennedy, D. Schoeberle, Quasi-Eulerian finite element formulation for fluid structure interaction, J. Press. Vess. Technol. 102 (1980) 62–69.
[5] T. Belytschko, W.K. Liu, B. Moran, Nonlinear Finite Elements for Continua and Structures, John Wiley & Sons, Inc., 2000.
[6] C. Bernardi, Y. Maday, A.T. Patera, Domain decomposition by the mortar element method, Asymptot. Numer. Methods Partial Differ. Equations 384 (1993) 269–286.
[7] C. Bernardi, Y. Maday, A.T. Patera, A new nonconforming approach to domain decomposition: the mortar element method, Nonlinear Partial Differ. Equations Appl. 299 (1994) 13–51.
[8] J. Chessa, The extended finite element method for free surface and two-phase flow problems, Ph.D. thesis, Northwestern University, June 2003.
[9] F. Cirak, R. Radovitzky, A Lagrangian–Eulerian shell-fluid coupling algorithm based on level sets, Comput. Struct. 83 (6–7) (2005) 491–498.
[10] C. Daux, N. Moës, J. Dolbow, N. Sukumar, T. Belytschko, Arbitrary cracks and holes with the extended finite element method, Int. J. Numer. Methods Engrg. 48 (12) (2000) 1741–1760.
[11] J. De Hart, G.W. Peters, P.J. Schreurs, F.P. Baaijens, A two-dimensional fluid–structure interaction model of the aortic value, J. Biomech. 33 (9) (2000) 1079–1088.
[12] J. Donéa, P. Fasoli-Stella, S. Giuliani, Lagrangian and Eulerian finite element techniques for transient fluid–structure interaction problems, in: Trans. 4th Int. Conf. on Structural Mechanics in Reactor Technology, 1977.
[13] R.P. Fedkiw, T. Aslam, B. Merriman, S. Osher, A non-oscillatory Eulerian approach to interfaces in multimaterial flows (the ghost fluid method), J. Comput. Phys. 152 (2) (1999) 457–492.
[14] C. Förster, W.A. Wall, E. Ramm, On the geometric conservation law in transient flow calculations on deforming domains, Int. J. Numer. Methods Fluids 50 (12) (2006) 1369–1379.
[15] C. Förster, W.A. Wall, E. Ramm, Artificial added mass instabilities in sequential staggered coupling of nonlinear structures and incompressible viscous flows, Comput. Methods Appl. Mech. Engrg. 196 (7) (2007) 1278–1293.
[16] C. Geuzaine, J.-F. Remacle, Gmsh: a three-dimensional finite element mesh generator with built-in pre- and post-processing facilities, 2007. http://www.geuz.org/gmsh/.
[17] R. Glowinski, T.-W. Pan, T.I. Hesla, D.D. Joseph, A distributed Lagrange multiplier/fictitious domain method for particulate flows, Int. J. Multiphase Flow 25 (5) (1999) 755–794.
[18] R. Glowinski, T.-W. Pan, J. Periaux, A fictitious domain method for external incompressible viscous flow modeled by Navier–Stokes equations, Comput. Methods Appl. Mech. Engrg. 112 (1–4) (1994) 133–148.
[19] A. Hansbo, P. Hansbo, A finite element method for the simulation of strong and weak discontinuities in solid mechanics, Comput. Methods Appl. Mech. Engrg. 193 (33–35) (2004) 3523–3540.
[20] C. Hirth, A.A. Amsden, J. Cook, An Arbitrary Lagrangian–Eulerian computing method for all flow speeds, J. Comput. Phys. 14 (1974) 227–253.
[21] T.J. Hughes, W.K. Liu, Implicit–explicit finite elements in transient analysis, J. Appl. Mech. 45 (1978) 371–378.
[22] T.J. Hughes, W.K. Liu, T. Zimmermann, Lagrangian–Eulerian finite element formulation for incompressible viscous flows, Comput. Methods Appl. Mech. Engrg. 29 (1981) 329–349.
[23] B.M. Irons, R.C. Tuck, A version of the Aitken accelerator for computer iteration, Int. J. Numer. Methods Engrg. 1 (3) (1969) 275–277.
[24] L. Lee, R.J. LeVeque, An immersed interface method for incompressible Navier–Stokes equations, SIAM J. Scientific Comput. 25 (3) (2003) 832–856.
[25] A. Legay, J. Chessa, T. Belytschko, An Eulerian–Lagrangian method for fluid–structure interaction based on level sets, Comput. Methods Appl. Mech. Engrg. 195 (17–18) (2006) 2070–2087.
[26] R.J. LeVeque, D. Calhoun, Cartesian grid methods for fluid flow in complex geometries, in: L.J. Fauci, S. Gueron (Eds.), Computational Modeling in Biological Fluid Dynamics, IMA Volumes in Mathematics and its Applications, vol. 124, Springer-Verlag, 2001.
[27] R. Löhner, J.D. Baum, E. Mestreau, D. Sharov, C. Charman, D. Pelessone, Adaptive embedded unstructured grid methods, Int. J. Numer. Methods Engrg. 60 (3) (2004) 641–660.
[28] R. Mittal, G. Iaccarino, Immersed boundary methods, Ann. Rev. Fluid Mech. 37 (1) (2005) 239–261.
[29] D.P. Mok, Partitionierte Lösungsansätze in der Struktur- dynamik und der Fluid-Struktur-Interaktion., Tech. Rep. Ph.D. Thesis, Report No. 36, Institute of Structural Mechanics, University of Stuttgart (2001).

[30] D.P. Mok, W.A. Wall, Partitioned analysis schemes for the transient interaction of incompressible flows and nonlinear flexible structures, in: W. Wall, K.-U. Bletzinger, K. Schweizerhof (Eds.), Trends in Computational Structural Mechanics, CIMNE: Barcelona, 2001.
[31] N. Moës, E. Béchet, M. Tourbier, Imposing Dirichlet boundary conditions in the extended finite element method, Int. J. Numer. Methods Engrg. 67 (12) (2006) 1641–1669.
[32] N. Moës, J. Dolbow, T. Belytschko, A finite element method for crack growth without remeshing, Int. J. Numer. Methods Engrg. 46 (1) (1999) 131–150.
[33] W. Noh, CEL: a time-dependent two-space-dimensional coupled Eulerian–Lagrangian code, in: B. Alder, S. Fernbach, M. Rotenberg (Eds.), Methods in Computational Physics, vol. 3, Academic Press, New York, 1964.
[34] K.C. Park, C.A. Felippa, R. Ohayon, Partitioned formulation of internal fluid–structure interaction problems by localized Lagrange multipliers, Comput. Methods Appl. Mech. Engrg. 190 (24–25) (2001) 2989–3007.
[35] C.S. Peskin, Numerical analysis of blood flow in the heart, J. Comput. Phys. 25 (3) (1977) 220–252.
[36] C.S. Peskin, The immersed boundary method, Acta Numer. 11 (1) (2002) 479–517.
[37] J. Réthoré, A. Gravouil, A. Combescure, An energy-conserving scheme for dynamic crack growth using the extended finite element method, Int. J. Numer. Methods Engrg. 63 (5) (2005) 631–659.
[38] M. Schäfer, S. Turek, Benchmark computations of laminar flow around a cylinder, Notes Numer. Fluid Mech. 52 (1996) 547–566.
[39] T.E. Tezduyar, Interface-tracking and interface-capturing techniques for finite element computation of moving boundaries and interfaces, Comput. Methods Appl. Mech. Engrg. 195 (23–24) (2006) 2983–3000.
[40] R. van Loon, P.D. Anderson, F.P. Baaijens, F.N. van de Vosse, A three-dimensional fluid–structure interaction method for heart valve modelling, CR Mec. 333 (12) (2005) 856–866.
[41] G.J. Wagner, S. Ghosal, W.K. Liu, Particulate flow simulations using lubrication theory solution enrichment, Int. J. Numer. Methods Engrg. 56 (9) (2003) 1261–1289.
[42] W.A. Wall, Fluid-Struktur-Interaktion mit stabilisierten Finiten Elementen, Ph.D. thesis, Universität Stuttgart, Institut für Baustatik, 1999.
[43] W.A. Wall, A. Gerstenberger, P. Gamnitzer, C. Förster, E. Ramm, Large deformation fluid–structure interaction – advances in ALE methods and new fixed grid approaches, in: H.-J. Bungartz, M. Schäfer (Eds.), Fluid–Structure Interaction: Modelling, Simulation, Optimisation, LNCSE, Springer-Verlag, 2006.
[44] W.A. Wall, D.P. Mok, E. Ramm, Partitioned analysis approach of the transient coupled response of viscous fluids and flexible structures, in: W. Wunderlich (Ed.), Solids, Structures and Coupled Problems in Engineering, Proc. ECCM'99, Munich, 1999.
[45] X. Wang, W.K. Liu, Extended immersed boundary method using FEM and RKPM, Comput. Methods Appl. Mech. Engrg. 193 (12–14) (2004) 1305–1321.
[46] B.I. Wohlmuth, Discretization Methods and Iterative Solvers Based on Domain Decomposition, Springer, 2001.
[47] Z. Yu, A DLM/FD method for fluid/flexible-body interactions, J. Comput. Phys. 207 (1) (2005) 1–27.
[48] L. Zhang, A. Gerstenberger, X. Wang, W.K. Liu, Immersed finite element method, Comput. Methods Appl. Mech. Engrg. 193 (21–22) (2004) 2051–2067.